molecular pharmaceutics

pubs.acs.org/molecularpharmaceutics Article

Diffusion and Exchange Kinetics of Microparticle Formulations by Spatial Fourier Transform Fluorescence Recovery after Photobleaching with Patterned Illumination

Jiayue Rong, Dustin Harmon, Ziyi Cao, Yang Song, Lu Zeng, and Garth J. Simpson*

Cite This: *Mol. Pharmaceutics* 2024, 21, 5539−5550 Read Online

ACCESS | Metrics & More | Article Recommendations | SI Supporting Information

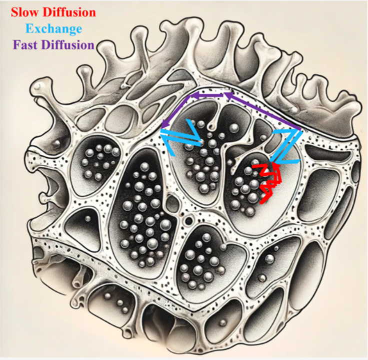

ABSTRACT: The mechanism of active pharmaceutical ingredient (API) mobility during release in microparticle formulation was investigated using periodically structured illumination combined with spatial Fourier transform fluorescence recovery after photobleaching (FT-FRAP). FT-FRAP applies structured photobleaching across a given field of view, allowing for the monitoring of molecular mobility through the analysis of recovery patterns in the FT domain. Encoding molecular mobility in the FT domain offers several advantages, including improved signal-to-noise ratio, simplified mathematical calculations, reduced sampling requirements, compatibility with multiphoton microscopy for imaging API molecules within the formulations, and the ability to distinguish between exchange and diffusion processes. To prepare microparticles for FT-FRAP analysis, a homogeneous mixture of dipyridamole and pH-independent methyl methacrylate polymer (Eudragit RS and RL) was processed using laminar jet breakup induced by vibration in a frequency-driven encapsulator. The encapsulated microparticles were characterized based on particle size distribution, encapsulation efficiency, batch size, and morphology. Utilizing FT-FRAP, the internal diffusion and exchange molecular mobility within RL and RS microparticles were discriminated and quantified. Theoretical modeling of exchange- and diffusion-controlled release revealed that both RL and RS microparticles exhibited similar exchange decay rates, but RL displayed a significantly higher diffusion coefficient. This difference in diffusion within RL and RS microparticles was correlated with their macroscopic dissolution performance.

KEYWORDS: *gastrointestinal tract, quaternary ammonium, temporal and spatial resolution*

1. INTRODUCTION

Oral administration is often the most convenient method for delivering APIs to patients, primarily due to its high patient compliance and versatile design options compared with intravital delivery. When an API is administered orally, it is crucial for solid APIs to exhibit an appropriate dissolution profile in the gastrointestinal (GI) tract to facilitate the desired absorption into the bloodstream. Controlled-release API delivery systems utilizing poly(acrylic acid) derivatives[1−3] prove highly effective in achieving specific time- and/or pH-dependent dissolution profiles within the GI tract.[4,5] Eudragit RL and RS are frequently employed as matrices or coating materials in time-controlled API delivery systems.[6] Eudragit RS contains approximately half the quantity of quaternary ammonium groups compared to Eudragit RL.

Despite the extensive use of Eudragit RL and RS in controlled-release oral API delivery, challenges remain in elucidating the mechanisms and kinetics involved in API release due to the potential complexity of the system. For instance, the fundamental interactions between the API and the polymer, as well as the API release dynamics within Eudragit RS and RL microparticles, are often insufficiently characterized. Furthermore, the presence of specific ions (e.g., quaternary ammonium) within the bulk solution and at the interface between microparticles and the surrounding liquid can potentially exert a significant influence on API−polymer interactions and, consequently, on the API release process.

To assess the controlled-release performance of microparticles, the diffusion of water into and API molecules out of polymer matrices is often evaluated.[7−9] The conventional approach involves determining API diffusion coefficients by fitting dissolution data to Fick's laws, assuming a direct linear relationship between API diffusion and dissolution.[7,10] However, several factors, such as surface heterogeneity of microparticles and additional modes of mobility beyond bulk diffusion, can introduce complexity into the relationships between the dissolution-derived API diffusion coefficients. Even when diffusion is considered the primary mode of

Received: May 7, 2024
Revised: July 30, 2024
Accepted: July 31, 2024
Published: October 10, 2024

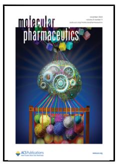

ACS Publications

https://doi.org/10.1021/acs.molpharmaceut.4c00508

mobility, dissolution measurements face limitations in characterizing the intricate spatial and temporal interactions between APIs and polymers within microparticles, extending from the inner regions to the bulk environment. This limitation stems from the inability of dissolution measurements to track the in situ trajectories of APIs with high spatial and temporal resolution. Moreover, the diffusion coefficient of water into polymer matrices is regularly used as a surrogate for inferring the mobility of the API itself. This choice is due to the technical challenges associated with directly monitoring API diffusion. While theoretical work has explored correlating water uptake kinetics with observable diffusion in Eudragit thin films,[7,10] the indirect extrapolation of water uptake kinetics to API diffusion cannot account for surface and interfacial exchange effects between the matrix and the bulk environment in heterogeneous samples. Despite the availability of model formulations involving API-loaded Eudragit thin films, real-world industrial microparticle formulations tend to be more intricate, with three-dimensional (3D) shapes introducing variations between inner and outer regions.[8,9] The release of compounds in 3D complicates matters, rendering dissolution-derived diffusion coefficients insufficient for capturing the intricacies of API—polymer interactions within microparticles. Even when the assumptions of homogeneity and simple diffusion kinetics are met, a gap remains between studying water uptake and compound release as separate measurements and quantifying the kinetics of polymers, APIs, and API—polymer interactions simultaneously in heterogeneous samples, all while achieving microscopic-level temporal and spatial resolution.[7,10]

Due to its paramount importance in assessing the effectiveness of industrial microparticle formulations for human health and formulation design, significant research has been devoted to understanding the dynamics of API release. A key focus has been investigating API—polymer interactions. Various analytical techniques are commonly employed for studying two-dimensional (2D) API—polymer interactions, which can potentially be expanded to 3D microparticles. These techniques include linear vibrational spectroscopy (e.g., IR and Raman spectroscopy),[11] differential scanning calorimetry (DSC),[12] nuclear magnetic resonance (NMR) spectroscopy,[13] isothermal titration calorimetry (ITC),[14] and analytical ultracentrifugation (AUC) coupled with ultraviolet—visible (UV—vis) spectrometry.[15] Linear vibrational spectroscopy, such as infrared (IR) and Raman spectroscopy, can provide insights into the hydrogen bonding dynamics of functional groups and their characteristic vibrational modes, offering indications of API—polymer interactions. However, challenges arise due to overlapping and weak signals. Additionally, strong water absorption in the IR spectrum can obscure relevant signals, as the controlled-release process of microparticles occurs in a liquid environment designed to mimic the gastrointestinal tract. Raman spectroscopy, while less affected by water interference, faces signal-to-noise issues due to background interferences from fluorescence.[11] NMR spectroscopy, although valuable, possesses relatively lower sensitivity compared to other spectroscopic methods.[16] Solid-state NMR (ssNMR) spectroscopy, which offers improved sensitivity over liquid NMR, can provide correlation spectra to study amorphous dispersions. This capability aids in identifying site-specific API-carrier solid dispersion, directly impacting API bioavailability at the intermolecular level.[17] Traditional techniques like PXRD, DSC, and ITC have been used to study Eudragit RL and RS microparticles under dry conditions.[12] However, characterizing API—polymer interactions in aqueous media, a necessity for controlled-release microparticles, limits the application of PXRD and DSC. While PXRD is the "gold standard" for identifying crystalline materials, its analytical utility for polymer systems with weak long-range ordering are more limited.

Fluorescence recovery after photobleaching (FRAP) has gained prominence for characterizing the kinetics of individual API mobility due to its ability to probe diffusion through the monitoring of fluorescence intensity recovery.[18−21] The concept involves exposing a region of interest to a brief, high-intensity light pulse, resulting in suppression of the fluorescence in the photobleached area. As a result of the molecular mobility of both APIs and polymers, unbleached fluorophores migrate back into the irradiated region, leading to the recovery of the fluorescence intensity. Such measurements are most commonly performed with a tightly focused photobleach spot to speed recovery and minimize 1/f noise from instrument drift. Despite the advantages of single and multiphoton "point-bleach" FRAP in tracking molecular mobility, its widespread application in pharmaceutical analysis is limited by several factors.[22] First, it typically requires precise knowledge of the point photobleaching beam profile for accurate diffusion determination, which can be subject to change following calibration by changes in the focal plane, aberrations, and the like. Second, conventional point-bleach FRAP is challenging to integrate with two-photon excitation due to local heating.[23] As such, the advantages of two-photon excited fluorescence (TPEF) for imaging through turbid, heterogeneous media such as tissue and microparticles are difficult to leverage in point-bleach FRAP analyses.[24] Third, the integrated signal power in point-bleach FRAP is limited by the finite number of fluorophores that can be bleached within a diffraction-limited location.

Spatial Fourier transform (FT) FRAP was developed by Geiger et al. to address the limitations of conventional point FRAP.[25] In FT-FRAP, photobleaching power is distributed throughout the field of view using periodically patterned illumination. Both "comb" patterns,[25] consisting of a periodically spaced series of lines, and "dot-array" 2D periodic patterns of repeating dots have been demonstrated in prior work.[26] In both instances, analysis in the spatial FT domain recovers sharp puncta with the potential for substantially greater integrated power than point-bleach FRAP. The compatibility of FT-FRAP with beam-scanning microscopy supports comb-photobleach patterning in both multiphoton excitation and confocal detection through simple control of the slow-scan axis. Furthermore, the time-dependent recovery scales with harmonic spacing rather than the point-spread function, removing potential impacts from uncertainties in the beam profile. Spatially resolved diffusion recovery within domains of arbitrary shape was shown through image segmentation analysis.[27] For species diffusing fast enough to recover significantly during the photobleaching process, FT-FRAP has been adapted to support fluorescence recovery while photobleaching.[29]

In this study, we deployed FT-FRAP to characterize molecular mobility within Eugradit RL and RS microparticles prepared with dipyridamole and connect microscopic mobility with macroscopic dissolution kinetics. Specifically, FT-FRAP was performed using Nile red as a local fluorescence reporter. Multiphoton excitation minimized potential complications from optical scattering.[24] Spatial FT analysis with periodically patterned photobleaching supported precise recovery measurements over multiple discrete distance scales in a single

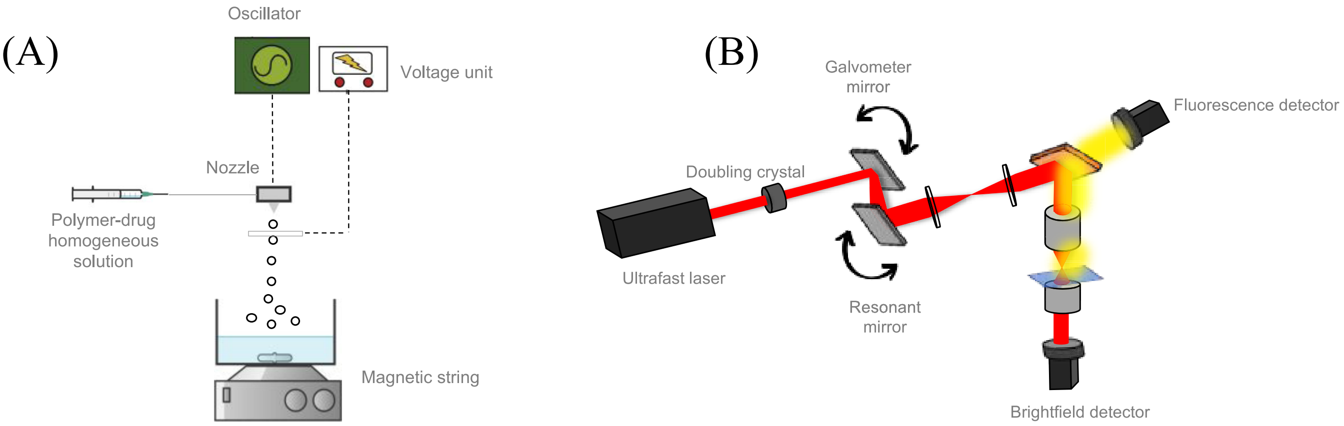

Figure 1. Schematic representations for the sample preparation and kinetics monitoring: Buchi encapsulator (A) and beam-scanning system for multiphoton excited FT-FRAP (B).

experiment.[25] Results of this analysis and implications for the mechanisms of recovery are discussed.

2. MATERIALS AND METHODS

2.1. Materials. Dipyridamole, Nile red, paraffin oil, and sorbitan sesquioleate were purchased from Sigma-Aldrich Inc. Eudragit RL 200 and RS 100 were donated by Evonik Corporation (Piscataway, NJ 08854). Methanol (J.T. Baker) was used as received. Dipyridamole was chosen as a model API since it has been widely used as a blood thinner and vasodilator to prevent blood clots, strokes, and heart attacks. However, due to its narrow therapeutic concentration range and meal-dependent absorption, managing the dose of this API has been rather difficult. The absorption of API from a conventional matrix tablet is strongly influenced by its residence time in the GI tract.

2.2. Preparation of the RL and RS Microparticle Formulation for Oral Delivery. The experimental scheme for the production of the microparticle formulation used in this study is depicted in Figure 1A. A homogeneous solution was prepared by dissolving 1g of dipyridamole and 10 g of Eudragit RL or RS in 389 mL of methanol with 11 mL of 1 mg/mL Nile red fluorescence labeling solution. The theoretical API loading is 9.09% by mass. Microparticles were prepared using a frequency-driven Buchi encapsulator (Flawil, Switzerland). Nozzles with diameters of either 300 or 450 μm were mounted. A homogeneous solution (150 mL) was extruded into a syringe. For both 300 and 450 μm nozzles, an oscillation frequency of 500 Hz was used to induce jet breakup of the dipyridamole polymer homogeneous solution into microparticles. The flow rate was 7 mL/min, and the voltage to separate microparticles was 700 V.

Microparticles were collected in paraffin (300 g) containing 1% (w/w) sorbitan sesquioleate (Span 83) as an emulsifier under agitation. Methanol was removed by stirring overnight. Paraffin oil was removed by centrifugation (3000 rpm, 8 min, 23°, 5 ACC) and washed three times with *n*-hexane (500 rpm, 2 min, 23°, 5 ACC). Hard microparticles were harvested by overnight drying, followed by acoustic sieving in LabRAM II (Butte). The microparticles were stored at room temperature.

2.3. Solid-State Characterization to Assess Particle Size, Morphology, Encapsulation Efficiency, and Batch Yield. The particle sizes of the RL and RS microparticles were measured by dynamic light scattering using a Horiba LA-950 (Kyoto, Japan). Microparticles were suspended in DI water. The average size of microparticles is expressed as a median diameter (D_{50}) and represents a particle diameter at 50% cumulative volume. Particle sizes were also evaluated by optical and scanning electron microscopy (SEM). For SEM studies, microparticles were adhered to carbon discs and platinum-coated using an EMITEC K550 sputter coater for 3 min at 40 mA. After coating, the samples were transferred to a Philips XL20 scanning electron microscope for imaging.

The encapsulation efficiency was determined by dissolving 5 mg of microparticles in 5 mL of 1:1 HPLC-grade H_2O:acetonitrile (ACN). As a model API, 10 mg of dipyridamole was dissolved in a 50 mL volumetric flask using the 1:1 HPLC-graded H_2O:ACN mobile phase. Samples were analyzed by high-performance liquid chromatography with ultraviolet detection (HPLC-UV). The experiment was replicated three times for each sample for statistical determination of the API loading percentage and encapsulation efficiency.

2.4. *In Vitro* Dissolution Testing on Microparticles. API release studies were conducted under sink conditions by employing a pH-varying method using an Agilent 708-DS dissolution apparatus with a paddle configuration. RL and RS microparticles, equivalent to 5.00 mg of dipyridamole concerning encapsulation efficiency, were weighed and placed in a glass vessel containing 500 mL of citrate acid buffer at pH 3.0. After 2 h, 1 M NaOH solution was added to adjust the pH to 6.2. The paddle speed was set at 100 rpm, and the solution temperature was maintained at 37.0 ± 0.5 °C. The tests lasted for 7 h, and each dissolution test was performed in triplicate.

Dipyridamole release was determined using an Agilent HPLC 1260 equipped with a UV detector at 254 nm. The reverse phase column (C18, 2.6 μm, 100 mm × 2.1 mm) was kept at 25 °C. The flow rate of the mobile phase (95% H_2O + 0.05% trifluoroacetic acid (TFA) with 5% ACN + 0.035%TFA) was 0.2 mL/min. Dipyridamole in ACN was used for calibration.

2.5. Classification and Quantification of Exchange and Diffusion Kinetics by FT-FRAP. The experimental scheme for the multiphoton excited FT-FRAP microscope used in this study is depicted in Figure 1B. A 50 MHz laser was used as the excitation source (Fianium, 1060 nm, 150 fs, <400 mW). The fundamental beam was raster-scanned across the sample using an 8.8 kHz resonant scanning mirror for the fast-scan axis and a galvanometer for the slow-scan axis. In normal imaging mode, the ramp function drives the galvanometer (slow axis) at 512 lines, along with the resonant mirror (fast axis). In photo-

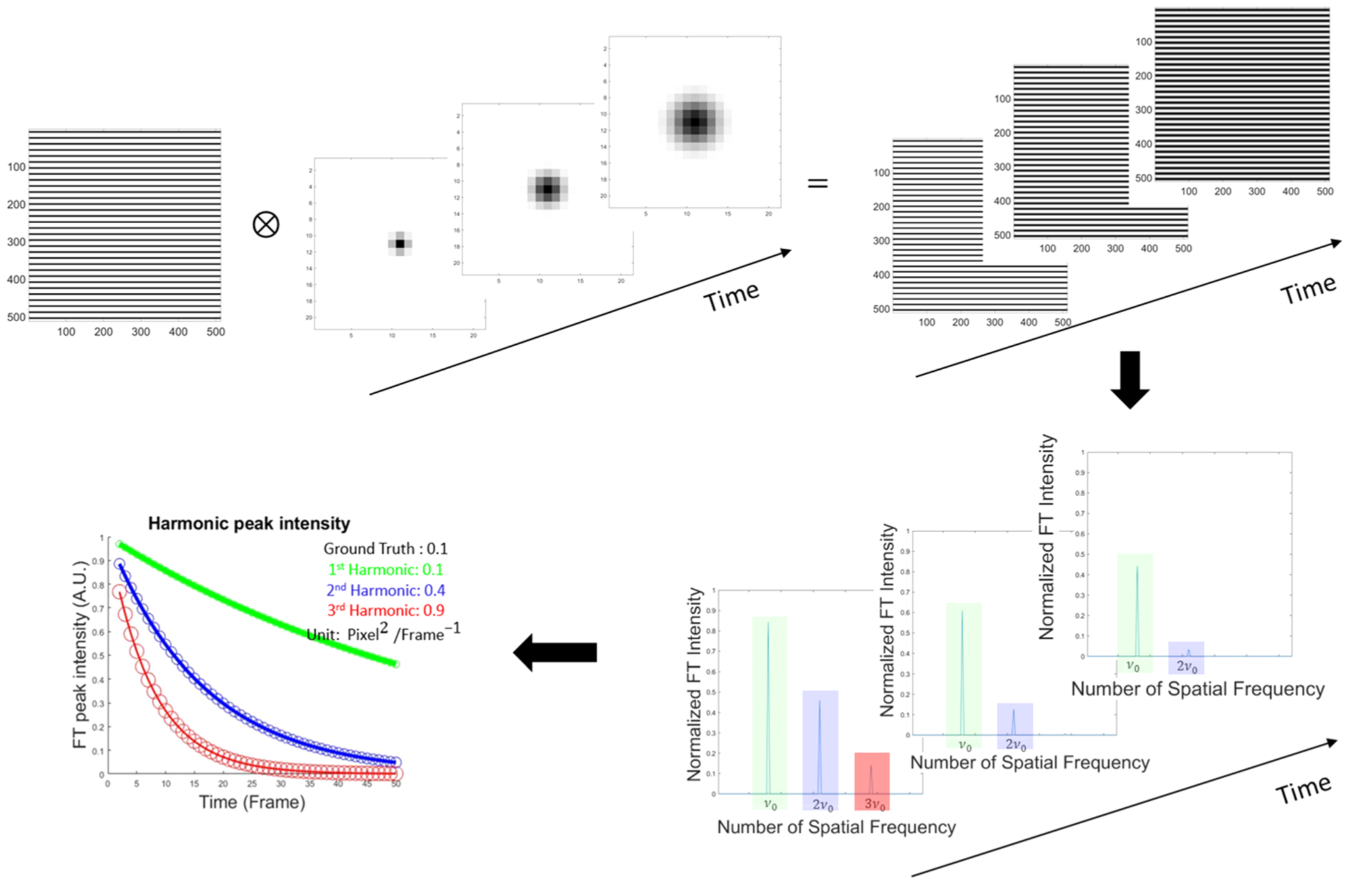

Figure 2. Schematic simulation overview of FT-FRAP implementation and analysis. The top left illustrates recovery modeled as the initial concentration gradient convolved with an ever-broadening Gaussian function over time. The spatial Fourier transformation of the time-varying periodic patterns produced a set of harmonic peaks at each time point, with the higher spatial frequencies decaying faster than the lower-order peaks. Integration of the harmonic peaks yielded exponentially decaying amplitudes, providing insights into molecular mobility.

bleaching mode, a "comb" photobleach pattern was induced by changing the ramp function to drive the galvanometer at 32 lines, corresponding to the fundamental spatial period. The normal and photobleaching modes were customized on a commercial Formulatrix Second Order Nonlinear Imaging of Chiral Crystals (SONICC) instrument for FT-FRAP measurements. A chamber with a controlled environment for *in situ* testing (CEiST)[30] was used for maintaining temperature and humidity during the API release of microparticles. Scheduled sampling with robotically controlled positioning supported the acquisition of parallel measurements of multiple sample wells continuously for time periods extending from minutes to hours.

A patterned comb bleach with 32 lines in a 512 × 512 image was used throughout these investigations. For a field of view (FoV) of 915 μm × 915 μm, the interline spacing (x_0) was $x_0 = \frac{\text{FoV}}{\text{lines of bleach}} = \frac{915\ \mu\text{m}}{32} = 28.59\ \mu\text{m}$, corresponding to a fundamental spatial frequency ($\tilde{\nu}_0$) of $\tilde{\nu}_0 = \frac{1}{x_0} = \frac{1}{28.59\ \mu m} = 0.035\ \mu m^{-1}$.

The time-lapse fluorescence images were analyzed by custom software written in MATLAB. A 2D spatial FT was applied to each image in the time series. The power spectrum given by the integrated magnitude of the Fourier domain peak was measured at each time point of the FT time-lapse, followed by integration over the peaks at the fundamental frequency ($\tilde{\nu}_0$= 32 μm^{-1}) and the second harmonic ($2^*\tilde{\nu}_0$ = 64 μm^{-1}). The integrated peak intensities during time series were fitted to a simple exponential decay model in eq 1 at each harmonic, where $\tilde{A}_n$ is the amplitude of the nth harmonic in the spatial FT domain, D is the diffusion coefficient, and k_{off} is the rate constant for exchange. The expression in eq 1 originates from the solution to Fick's law of diffusion, evaluated in the spatial Fourier transform domain to include both distance-dependent diffusive and distance-independent exchange recovery mechanisms, as detailed in Cao et al.[27]

$$\tilde{A}_n(t) = \tilde{A}_n(0)e^{-(4\pi^2\tilde{\nu}_0^2 D + k_{\text{off}})t} \tag{1}$$

Interfacial exchange and bulk diffusion contributions were recovered by decomposing the set of decays with eq 2, reproduced from Cao et al.[27] In eq 2, each k_n term corresponds to the observed exponential decay coefficient for the nth harmonic peak in the spatial Fourier transform domain, which includes both harmonic-dependent diffusion contributions and harmonic-independent exchange contributions. Uncertainties in the diffusion and exchange coefficients were propagated from uncertainties in the fits to recover k_n for each harmonic.

$$\begin{bmatrix} k_1 \\ k_2 \\ k_3 \\ \vdots \end{bmatrix}_{\text{obs}} = \begin{bmatrix} 1 & 1 \\ 4 & 1 \\ 9 & 1 \\ & \vdots \end{bmatrix} \begin{bmatrix} 4\pi^2\overline{v}_0^2 D_A \\ k_{\text{off}} \end{bmatrix} \tag{2}$$

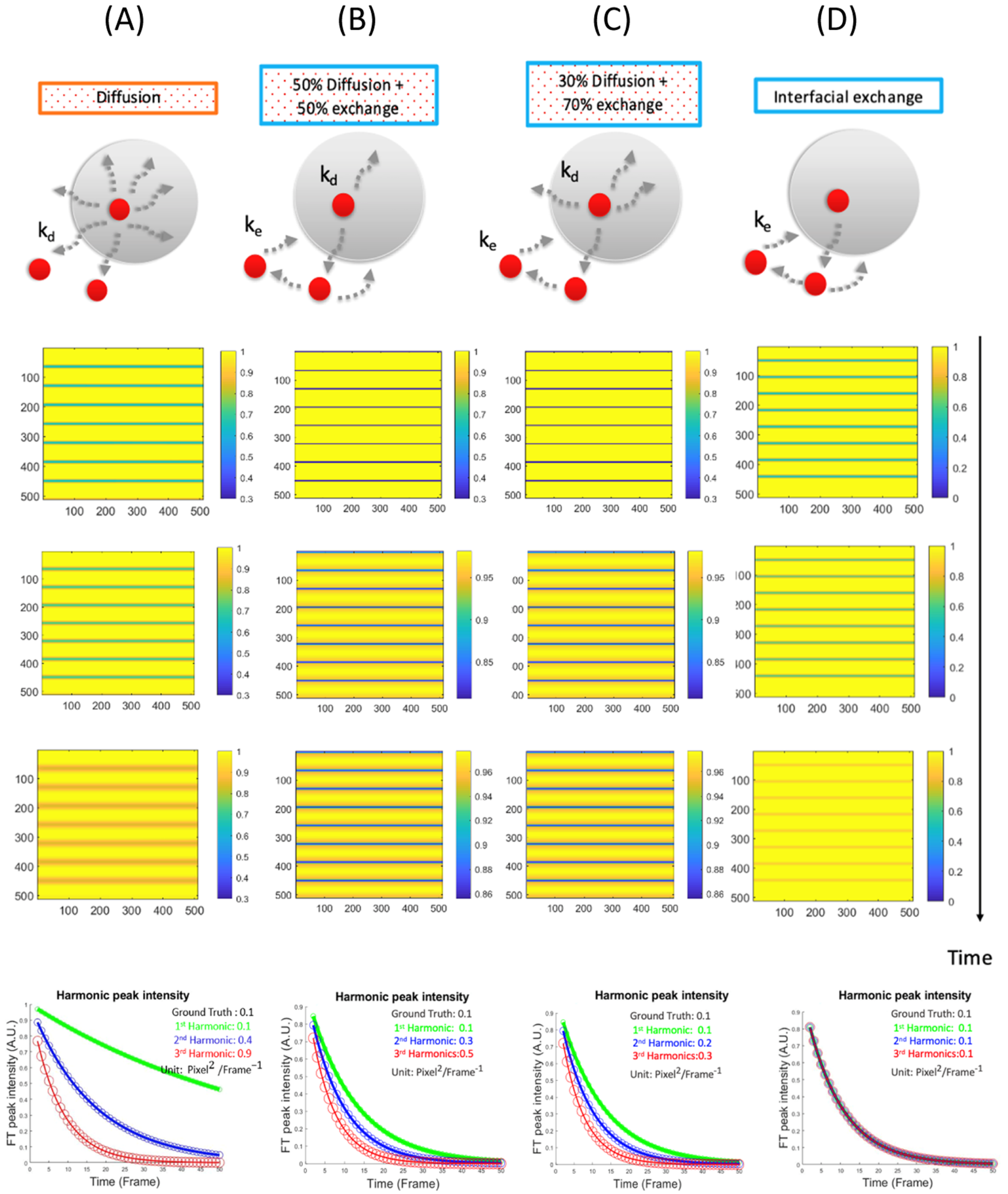

Figure 3. Schematic representations (top row) and simulated FT-FRAP measurements (middle row) of diffusion- and exchange-controlled release. Diffusion-controlled release exhibits broadening of the comb pattern with diffusion (bottom left). In contrast, interfacial-exchange-controlled release retains the original sharp features, decaying only in amplitude during recovery (bottom right). Multiharmonic analysis facilitates decomposition of diffusion and exchange contributions through the combination of recoveries at multiple specific distance scales.

Simulations shown in Figure 2 illustrate the experimental pipeline of the FT-FRAP approach. Mobility was modeled by a time-variable Gaussian point-spread function. The scanning pattern was modeled by using a comb periodic mask. The time-lapse measurements were correspondingly given by a convolution of a time-varied Gaussian filter with the initial comb patterns (or, equivalently, repeated sequential filtering with the same Gaussian kernel). In the spatial Fourier transform domain, the convolution operations in real space transform to multiplication in Fourier space. By recording the intensity of the puncta corresponding to spatial harmonics over time, we can extract the diffusion and exchange coefficients from the recovery kinetics.

2.6. Simulations of Dual Kinetics with Multiharmonics Analysis.

To evaluate the multiharmonics analysis outlined in eq 1 and eq 2, simulations of diffusion-only, exchange-only, and both diffusion and exchange kinetics are presented in Figure 3 using MATLAB. For diffusion, the initial images were multiplied by a comb pattern mask representing the point-spread function and the photobleaching profile. The exchange was represented by $1-e^{k_{\mathrm{off}}\Delta t}$. All analyses were performed in the spatial Fourier domain. The "ground truth" decay value for either diffusion or exchange was set to $1 \times 10^{-2} - 1 \times 10^{-3}$ s^{-1} to encompass the experimental results.

Prior to the FT analysis for the comb-bleached FRAP experimental measurements, the theoretical exchange and diffusion dual kinetics model developed based on the FT-FRAP approach were simulated, as shown in Figure 3. Simulations included recovery from bulk diffusion and exchange-mediated recovery with invaginating aqueous channels of comparatively high mobility, the results of which are shown in Figure 3A–D (top row). For diffusion-only kinetics in Figure 3A, the API was assumed to release from microparticles driven by normal diffusive motion. Therefore, the recovery times were purely dependent on D in eq 1. By plotting the intensities of nth harmonics, the multiharmonics analysis showed the recovered nth diffusion coefficients followed n^2 dependence on the order of the corresponding harmonic peak (e.g., second and third harmonics recovered fourfold and ninefold faster decays relative to the fundamental spatial frequency), consistent with expectations for normal diffusion.[25,27]

Upon uptake of water, it is reasonable to assume the presence of interfacial layers on the surfaces of the Eudragit RL and RS polymers, exhibiting different effective viscosities from those within the bulk. Higher interfacial mobility could arise from molecular partitioning to the interface or due to the formation of an interfacial gel layer with reduced viscosity, as illustrated in Figure 3D. In this model, the rate of recovery is dictated by the bottleneck rate of local transport from the bulk to exchange within the interfacial layer, after which the mobility is relatively fast. Deviations from normal diffusion depicted in Figure 3A can arise through this exchange mechanism (Figure 3D). For exchange-only kinetics, the slow step of exchange from the bulk to the higher-mobility interfacial layer produces identical decay rates for all nth harmonics, as the recovery is assumed to be relatively fast following exchange events. In general, both lateral diffusion within the polymer bulk and interfacial exchange are likely to contribute to the recoveries; analysis in Fourier space can decompose contributions from both diffusion and exchange mobility, as described in eq 2. Simulations of recovery curves exhibiting both diffusion and exchange contributions are shown in Figure 3B,C. Collectively, the FT analysis of diffusion-only, exchange-only, and dual kinetics simulations provides a mathematical foundation to decompose the bulk and interfacial mobility for the release of dipyridamole from swelling-based Eudragit microparticles.

3. RESULTS AND DISCUSSION

A summary of size and composition characterizations is given in Table 1. Microparticle formulations of API and RL or RS polymers were prepared. For Eudragit RL microparticles, both the yield and encapsulation efficiency were >90%, irrespective of the polymer or nozzle size. The encapsulation formulation efficiency was ~90% for both RS and RL microparticles. The median sizes (D_{50}) of RL microparticles were generally larger than those of RS microparticles. The translational mobilities of API (dipyridamole) and its fluorescence reporter Nile red within the microparticle formulations were measured by multiphoton excited patterned FRAP within the controlled environment chamber, as described in Section 2.5. The quantification of the kinetics of the API with Nile red were performed by fitting integrated FT peaks of patterned FRAP measurements to exponential decays using eqs 1 and 2. With the patterned FRAP measurements and exponential fitting in the Fourier domain, the kinetics of API with Nile red within both RL and RS microparticles immersed in phosphate-buffered saline (PBS) were determined and are reported in Figures 4 and 5. Visualizations of the microparticles composed of dipyridamole and RL or RS polymers immersed in PBS are shown in Figures 4A and 5A. Representative recovery images in the time domain after photobleaching of microparticle formulations are shown in Figures 4B and 5B, and their peaks in the FT domain are shown in Figures 4C and 5C. Translation of Nile red within RL and RS microparticles was decomposed into diffusive and exchange contributions, as shown in Figures 4D and 5D. For the RL microparticles in Figure 4D, the second harmonic peaks decayed faster than the first harmonic peaks for RL microparticles. In contrast, RS microparticles in Figure 5D exhibited only subtle differences in the recovery curves for the first and second harmonics.

Table 1. Microparticle Size and Yield Characteristics[a]

polymer	nozzle	median size (μm) ± SD	encapsulation efficiency (%) ± SD	total yield (%) ± SD
Eudragit RL	300	121 ± 14	92 ± 2	95 ± 1
	450	132 ± 10	88 ± 2	98 ± 3
Eudragit RS	300	28 ± 5	86 ± 4	99 ± 1
	450	32 ± 2	87 ± 3	85 ± 3

[a] Standard deviations were evaluated using either three or four replicates.

This simultaneous monitoring of spatial harmonics at multiple length scales from the first and second harmonics suggested that the mobility of API and its hydrophobic fluorescent report is insufficiently recovered by consideration of diffusion alone. We hypothesize that the recovery includes contributions from interfacial mobility, as described by the exchange operation in the simulations depicted in Figure 3. As reported by Zhu et al.,[28] an enhanced mobility at the interfaces of molecular glasses can occur when the movement of API is faster within a high-mobility interfacial layer compared to the bulk solution; in such instances, the mobility rate is dominated by the "on" rate of exchange to the bulk solution and limited by the "off" rate of exchange back to the interfacial layer formed at the sample surface of the microparticles. Consistent with the simulation depicted in Figure 3 and in eq 1, kinetics dominated by the exchange mechanism are expected to show identical decay rates across all spatial harmonics. Kinetics dominated by diffusion, as derived by Fick's law, should scale with the square of

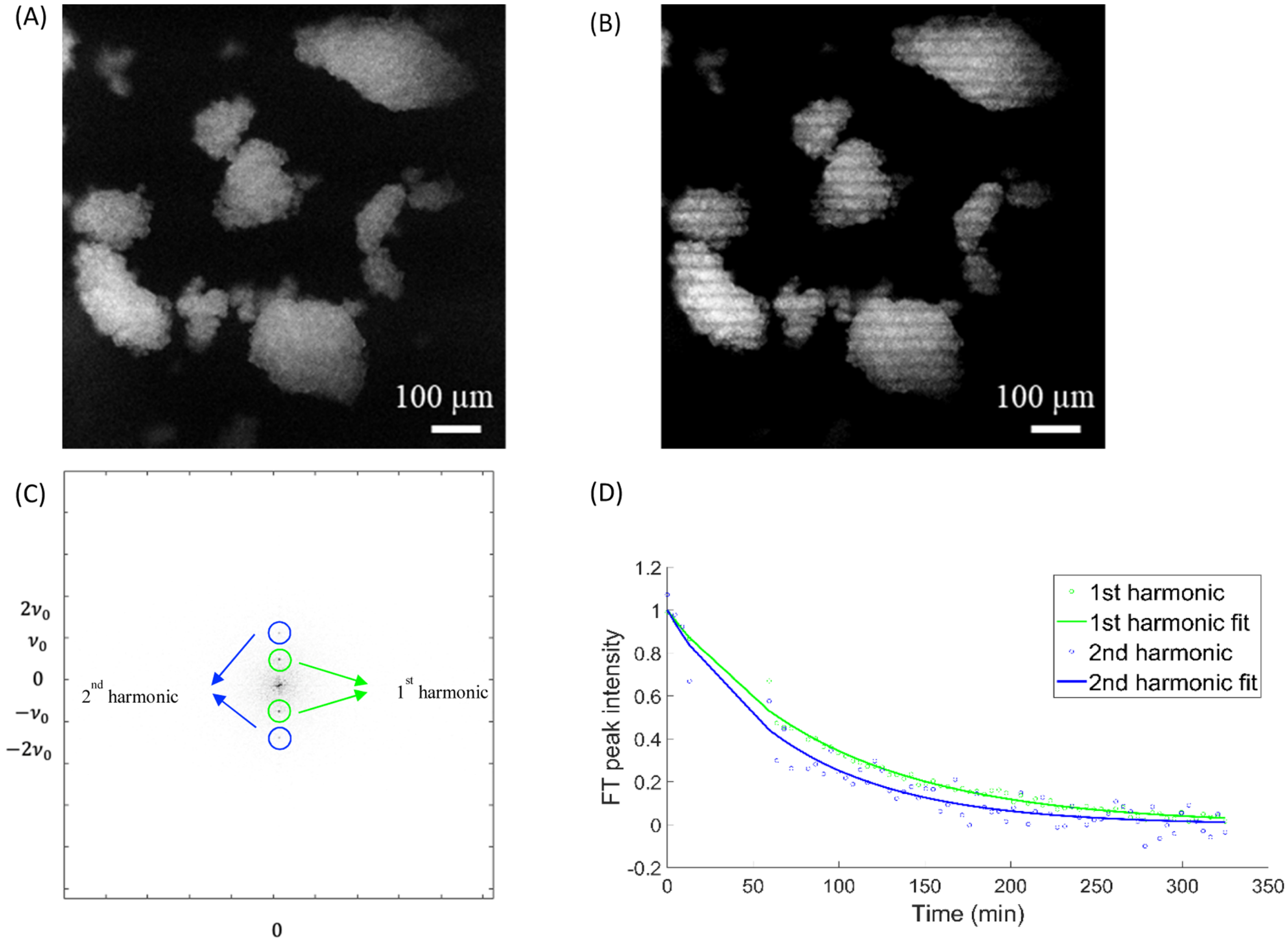

Figure 4. RL microparticles prior to (A) and shortly after (B) comb photobleaching. Spatial Fourier transformation of a representative postbleaching yields peak magnitudes (C), producing time-dependent peaks in the FT domain (D), along with exponential fits of the data.

the harmonic order in reciprocal space and therefore exhibit a steep distance dependence.[25,27] The exchange and diffusion kinetics were compared for RL and RS microparticles since FT-FRAP enabled the decomposition of the decay responses into exchange and diffusion components. The recovered decay exchange rate coefficients for RL and RS microparticles were remarkably similar, with RL microparticles producing a rate coefficient of 5×10^{-3} s^{-1} ± 1×10^{-3} s^{-1} ($N = 6$) and RS microparticles producing a rate coefficient of 6×10^{-3} s^{-1} ± 1×10^{-3} s^{-1} ($N = 6$). The diffusion coefficients of RL and RS microparticles were calculated from the decay rate and are presented in Figure 6. Analysis of variance arising from each individual experiment (i.e., standard error of the fit) and across multiple independent trials is shown in SI Figure S2, suggesting that the variability from independent replicates is significantly greater than the measurement uncertainty from FT-FRAP.

Diffusion coefficients were also recovered from parallel evaluation of the multiharmonic data, calculable based on the component in total recovery scaling with the squared harmonic number. Multiplication by a factor of $4\pi^2\nu^2$ was used to convert the recovery time to the diffusion coefficient. RL was found to have a diffusion coefficient of $7 \times 10^{-7} \pm 1 \times 10^{-7}$ cm^2/s. RS was found to have a diffusion coefficient of $1.7 \times 10^{-7} \pm 0.9 \times 10^{-7}$ cm^2/s. The diffusion coefficients of dipyridamole obtained for RL and RS were generally in good agreement with prior molecular diffusion measurements using RL and RS polymer matrices, prepared as thin films containing weakly basic model compound metoprolol as a free base.[7,10] In measurements by Glaessl and co-workers,[7,10] API diffusion was estimated based on water uptake rates, assuming that diffusivity increases linearly with absorbed water content. In these water sorption studies, the diffusion coefficients of water into thin Eudragit films containing metoprolol-free base were ~1.5×10^{-7} cm^2/s in 10% RL and ~0.50×10^{-8} cm^2/s in 10% RS thin films.[10] Despite the substantial difference in both approaches taken, the results of the FT-FRAP measurements for Nile red within RL and RS API formulations are within an order of magnitude of these prior results for water mobility and exhibit similar trends, showing higher mobility within the RL and RS polymer matrices.

To benchmark the total release kinetics of API in RL and RS microparticles, FT-FRAP measurements were complemented by a dissolution kinetics analysis. The dissolution was replicated a minimum of three times for both RL and RS microparticles. Dissolution data and their exponential fitting are shown in Figure 7. The RL microparticles exhibited exponential decay coefficients of 0.0303 ± 0.0019 min^{-1}, while RS microparticles exhibited exponential decay coefficients of 0.0094 ± 0.0002 min^{-1} based on nonlinear curve-fitting equation %dissolved(t) = 100%($1 - e^{-kt}$) to recover the decay coefficient k. According to this curve-fitting equation, the initial dissolution rate is approximately given by k. The fitting of the experimental

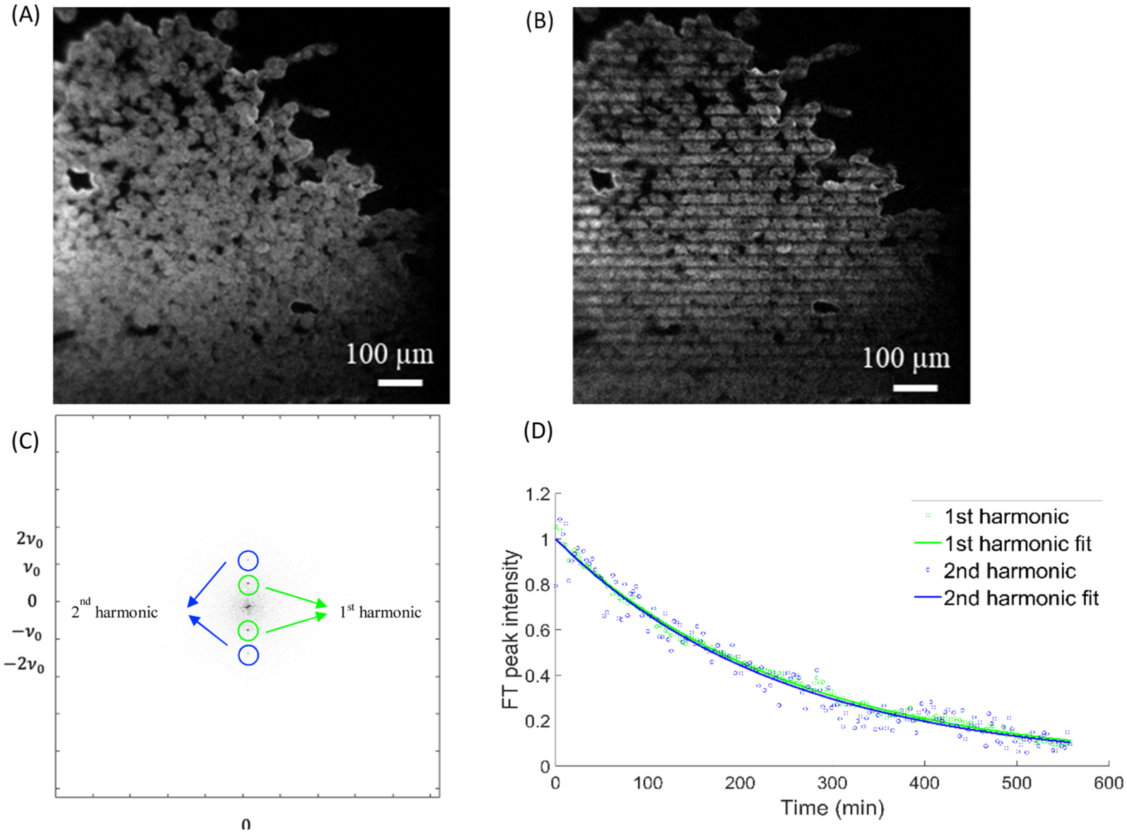

Figure 5. RS microparticles prior to (A) and shortly after (B) comb photobleaching. Spatial Fourier transformation of a representative postbleach yields peak magnitudes (C), producing time-dependent peaks in the FT domain (D), along with exponential fits of the data.

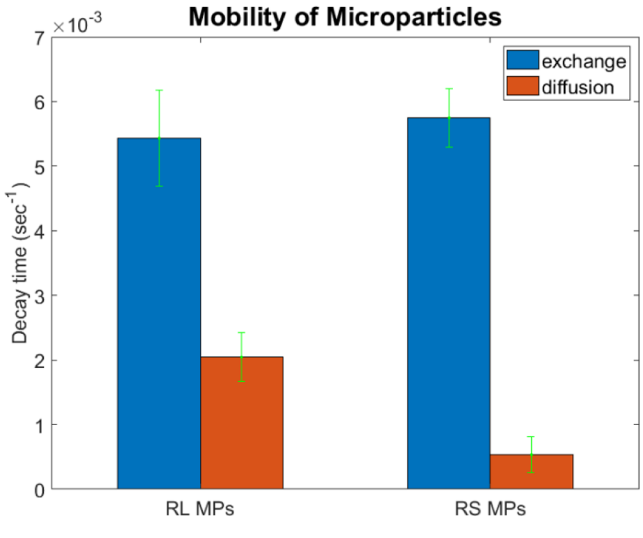

Figure 6. Decomposition of measured FT-FRAP multiharmonic recovery curves into diffusion and exchange contributions for in vitro dissolution of RL and RS microparticles.

dissolution data revealed a ∼3.22-fold difference in decay coefficients between RL and RS microparticles.

It was noticed that between the RL and RS microparticles, the diffusion decay ratio (∼3.82) and dissolution rate ratio (∼3.22) were comparable. Given their similarity, it is tempting to explore possible quantitative connections between diffusion-limited motion through the polymeric microparticle bulk and macroscopic dissolution rates. Correlations would be expected if the kinetics of dissolution exhibit bulk diffusion as the rate-limiting step. Consistent with this expectation, the recovery due to exchange was significantly faster for both microparticles than the recovery arising from bulk diffusion, suggesting that diffusion is rate-limiting.

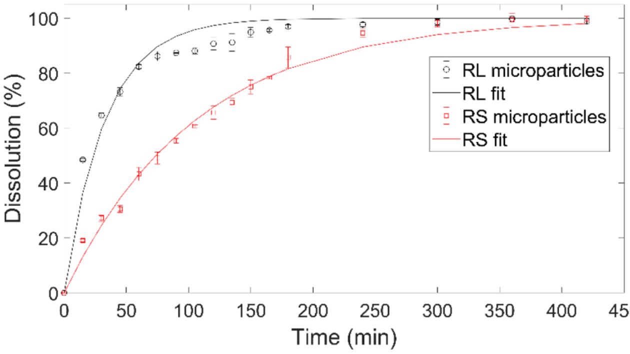

Figure 7. Stirred chamber dissolution kinetics for RL and RS microparticles (37.0 ± 0.5 °C, pH = 3.0 for 0 < time ≤120 min, pH 6.2 for time >120 min).

While the dominant effect connecting dissolution with bulk diffusion appears to be through diffusion-limited molecular translation within the RL and RS polymer matrices, the ratio of diffusion coefficients between RL and RS microparticles of ∼3.82 is statistically significantly different from the ratio of dissolution rates of ∼3.22. Several possible mechanisms were considered for the subtle difference in relative diffusion and dissolution rates between the two polymeric materials. The difference in average particle size between RL and RS particles was excluded as a significant factor controlling initial dissolution rates, as size-dependent dissolution has been shown to favor

https://doi.org/10.1021/acs.molpharmaceut.4c00508

smaller particles (in this case, RS), while larger RL particles exhibited faster dissolution kinetics. The average MW values do not differ significantly between the two polymers (MW(RL) ≅ MW(RS) ≅ 32,000 g/mol). Differences in the polymer chemical compositions were also considered. Based on the chemical composition of monomers, RL has a higher percentage of ammonium groups and correspondingly a higher aqueous permeability. Water can serve as a plasticizing agent in polymers by forming hydrogen bonds with hydroxyl groups and/or ammonium groups,[7] potentially providing a connection between the higher water sorption and increased molecular probe diffusivity in RL relative to RS.

Analysis of FT-FRAP also enabled independent quantification of the exchange kinetics, as shown in Figure 6. In noticeable contrast to the diffusion measurements, both RL and RS exhibited similar exchange kinetics (within experimental uncertainty of each other). On initial inspection, it may not be obvious how an interfacial exchange-based mechanism could be contributing to the observed recoveries within the nominal bulks of the particles accessed through multiphoton excitation. One might expect only the outer geometric surface to contribute to recovery through interfacial exchange. However, porous particles have the potential to exhibit substantial internal interfacial areas, which are directly accessible through multiphoton excitation. Arnold et al. reported the production of porous encapsulated microparticles when using oils as extractable pyrogens.[31] The findings from Arnold et al. support the phenomenon we attribute to the porous structure of encapsulation microparticles, which possess a significant internal surface area. Consistent with these prior studies, SEM measurements shown in SI Figure 1 reveal significant nanoscale structures within both RL and RS microparticles. These SEM data suggest the potential for substantial internal porosity, potentially supporting interfacial exchange within the nominal bulk volume of the microparticle, accessible through multiphoton FRAP analysis.

The use of multiphoton excitation to interrogate the bulk behavior of the microparticles was critical to understanding the molecular mobility and dissolution trends. Two-photon excited fluorescence (TPEF) enabled penetration into the microparticle cores,[24] which would be otherwise inaccessible using single-photon excitation due to optical scattering from heterogeneities within the highly turbid porous microparticle structures. Scattering losses may impact the overall intensity of the TPEF signal observed but generally do not degrade the image quality. Only the "ballistic" light surviving to the focal plane exhibits sufficient peak intensity to support TPEF. Furthermore, image quality is also not impacted by subsequent scattering of the visible fluorescence prior to detection since beam-scanning images are generated from the time-dependent signal. Using infrared light for TPEF greatly reduced scattering losses to enable optical cross sectioning of the microparticles. Optical penetration to the microparticle cores allowed access to the internal structures, which are also directly accessible by aqueous penetration throughout the porous particles upon immersion.

Given the relatively fast rate of exchange within the FT-FRAP analysis, it is potentially surprising that the exchange decay rate ratio does not correlate with the dissolution rate for RL and RS microparticles. A more detailed discussion of the kinetics of exchange suggests possible explanations for this disparity. The high contribution of exchange in both RL and RS microparticles, regardless of the chemical composition, suggests a significant surface area within the microparticles, consistent with the SEM results and prior studies detailed in the preceding paragraph. Internal surfaces within RL and RS microparticles with high-mobility interfacial phases can support exchange from highly viscous bulk material to higher-mobility interfacial layers. The two most likely mechanisms within these internal interfacial regions include (i) exchange to an interfacial layer tightly associated with the solid phase but with higher interfacial mobility and (ii) dissolution into confined solvent phases entrained within the bulk material. As a standalone method, FT-FRAP measurements cannot easily differentiate between these two limiting instances. Given the small volumes and relatively slow molecular transport at low Reynolds numbers in confined aqueous channels, the internal aqueous phase and/or the interfacial layer could quickly become saturated with API. Irrespective of whether the exchange arises to a high-mobility interfacial layer or to a (relatively) high-mobility confined bulk phase, the net effect is predicted to be similar; internal microstructure contributes to exchange-driven molecular transport within the RS and RL particles.

The strong correlation between probe molecule dissolution within the bulk and API dissolution kinetics is in good agreement with prior interpretations for bulk-diffusion-limited API release within the hydrated polymer. Lecomte et al. and Rongthong et al. have reported water acting as a potential plasticizer following sorption within the polymer, as Eudragit films, which are brittle in a dry state, become highly flexible when wetted.[32,33] Following Lecomte's work, Glaessl et al. conducted water uptake and dissolution experiments on Eudragit RL and RS API delivery films for correlation.[7,10] Glaessl directly fitted the API-releasing data based on the flask-shaking method into Fick's diffusion law to recover diffusion coefficients of API in Eudragit RL and RS API delivery systems.[7,10] In these studies, mobility of the API within the partially or wholly hydrated polymer matrices was inferred based on water uptake rather than directly measured as in the present study. The present study bolsters these mechanistic explanations through direct measurement of the relative mobilities of representative probe molecules rather than water sorption.

The observation of exchange-dominated FT-FRAP recovery may initially appear to be at odds with these prior bulk dissolution studies interpreted assuming bulk diffusion modeling. However, the microscopic and macroscopic measurements may potentially be bridged by the consideration of the role of water uptake within the polymer matrices. For polymers designed for swelling-induced release such as Eudragit RL and RS, API release is described by a two-step process:[33,34] (i) positively charged Eudragit RL and RS undergo significant swelling upon contact with water and form a gel layer;[35,36] and (ii) the gel layer acts as a diffusion barrier for the continued uptake of water.[37,38]

In this context, the combined measurements of diffusion and exchange may provide insights to bridge the gap between the two-step mechanism summarized by Rongthong et al.[33,35−38] and the bulk diffusion-controlled release by Glaessl et al.[7,10,34] The presence of an interfacial gel layer of viscosity lower than the bulk polymer is consistent with the exchange mechanism contributing to rapid internal recovery in the FT-FRAP measurements. However, if these interfaces are internal within porous media, local steady-state concentration of API within internal gel layers can result in fast exchange in FT-FRAP that does not necessarily correlate with release within the bulk solution, which can arise only from the externally exposed interface of the polymer particles. These results are consistent with the agglomerate structures of the polymeric matrices measured by SEM (Supporting Information), in which substantial internal surface area appears likely.

FT-FRAP with multiphoton excitation provides kinetics information unique and complementary to standard dissolution testing evaluations. Given the prominent role of exchange in FT-FRAP recovery of the probe molecule, we discovered that exchange contributions from a presumed interfacial layer appear to play a major role in driving the molecular mobility of hydrophobic probes within microparticulate agglomerations. It is perhaps counterintuitive that the relative macroscopic dissolution rates correlate well with the bulk diffusion coefficients, but not with interfacial exchange rates. We argue that this correlation ties back to the water uptake and swelling mechanism, supporting the mobility of both dissolution and bulk material diffusion. While the interface exchange is dominating the recovery inside the particles, bulk diffusion of the fluorescent probe is the rate-determining step for dissolution within microparticles, thus driving the mobility presented in the dissolution curve. This observation is in agreement with the release kinetics governed by bulk diffusion, which ties back to the water uptake and swelling mechanism.

FT-FRAP supports multiphoton excitation to access mobility within the internal particle matrix, separating bulk diffusion from internal interfacial exchange. In this study, the discrimination between exchange and diffusion explained the broad agreement between water uptake and direct measurements of molecular mobility by FT-FRAP.[7,10] Although the diffusion coefficients obtained assumed that water diffusion coefficients equate to API release diffusion coefficients, the high internal surface area, consistent with agglomerate formation, was shown to be critical for interpreting molecular mobility within porous pharmaceutical materials for controlled release. FT-FRAP not only enabled discrimination of exchange and diffusion but also offers benefits in microparticle characterization through multiphoton illumination and Fourier Transformation in addition to the FRAP method. For this study, we demonstrated the advantages of multiphoton excitation in accessing the interior regions within RS and RL particles without the complications of optical scattering. This access would be challenging without multiphoton excitation due to the intrinsic turbidity of the microparticles.

4. CONCLUSIONS

We demonstrated the quantitation and classification of diffusion and exchange kinetics using FT-FRAP on a representative industrial encapsulated microparticle formulation. The exchange rates showed no significant difference across polymer types or particle sizes. The exchange rate attributed to inhomogeneous surfaces of microparticles was confirmed by SEM. For the diffusion coefficients, Eudragit RL microparticles were ∼3.82 times faster than Eudragit RS microparticles. The higher diffusion coefficient in RL microparticles was hypothesized as being primarily attributed to the higher percentage of ammonia groups, which have a higher probability of forming hydrogen bonds with the liquid environment, which was supported by the ∼3.22 difference of dissolution coefficients characterized by dissolution testing.

The present study centered on changes just in the chemical composition of the polymer matrix with the molecular weight (MW) held constant for both RL and RS polymers. Variability in the MW can also profoundly impact diffusivity and API release, providing yet another parameter for optimization. Although beyond the scope of this study, the methods described herein should be equally applicable to studies designed to assess the role of MW in pharmaceutical material design.

In the present work, multiphoton FT-FRAP was shown to characterize the molecular mobility to determine the mechanisms of dissolution performance within encapsulation-based particulate formulations. Multiphoton excitation provided direct access to the internal microstructure environment within the bulk of the particles, which is challenging to isolate using conventional microscopy due to optical scattering. FT analysis offers substantial improvements in characterizing molecular mobility by distinguishing exchange and diffusion kinetics; it enhances the signal-to-noise ratio, simplifies mathematical calculations, requires low sampling, and is compatible with multiphoton microscopy for imaging API molecules within formulations. The ability to distinguish between exchange and diffusion using multiharmonic analysis provided an avenue to better understand the quantitative and qualitative API release kinetics in thick API delivery systems that are otherwise inherently challenging to study with traditional one-photon fluorescence methods due to scattering at deeper depths. The FT-FRAP modality, initially demonstrated in thin films,[27] was adapted with multiphoton excitation for 3D microparticles. By quantifying diffusion in microparticle formulations, dosage form optimization can be facilitated, product development can be accelerated, and troubleshooting during formulation design and production can be improved.

■ ASSOCIATED CONTENT

Supporting Information

The Supporting Information is available free of charge at https://pubs.acs.org/doi/10.1021/acs.molpharmaceut.4c00508.

> Reproducible FT-FRAP results of RL (left) and RS (right) microparticles; SEM results to support high interfacial mobility; analysis of spontaneous intensity blinking on RS microparticles; and label-free TPE-UVF results supporting crystallization (PDF)

■ AUTHOR INFORMATION

Corresponding Author

Garth J. Simpson − *Department of Chemistry, Purdue University, West Lafayette, Indiana 47907, United States;* orcid.org/0000-0002-3932-848X; Email: gsimpson@purdue.edu

Authors

Jiayue Rong − *Department of Chemistry, Purdue University, West Lafayette, Indiana 47907, United States*
Dustin Harmon − *Department of Chemistry, Purdue University, West Lafayette, Indiana 47907, United States*
Ziyi Cao − *Department of Chemistry, Purdue University, West Lafayette, Indiana 47907, United States;* orcid.org/0000-0002-7461-2902
Yang Song − *Takeda Pharmaceutics, Cambridge, Massachusetts 02139, United States*
Lu Zeng − *Takeda Pharmaceutics, Cambridge, Massachusetts 02139, United States*

Complete contact information is available at:
https://pubs.acs.org/10.1021/acs.molpharmaceut.4c00508

Notes

The authors declare no competing financial interest.

■ ACKNOWLEDGMENTS

The authors gratefully acknowledge funding from NSF-CIF-CCF-1763896, NSF-CHE-D3SC-2004046, and NSF-CHE-2305178. The authors also acknowledge support from the NSF Center for Bioanalytic Metrology (IIP-1916691). This research was supported in part through computational resources provided by Information Technology at Purdue University, West Lafayette, Indiana.

■ REFERENCES

(1) Albers, J.; Alles, R.; Matthée, K.; Knop, K.; Nahrup, J. S.; Kleinebudde, P. Mechanism of Drug Release from Polymethacrylate-Based Extrudates and Milled Strands Prepared by Hot-Melt Extrusion. *Eur. J. Pharm. Biopharm.* **2009**, *71* (2), 387−394.

(2) Semdé, R.; Amighi, K.; Devleeschouwer, M. J.; Moës, A. J. Studies of Pectin HM/Eudragit RL/Eudragit NE Film-Coating Formulations Intended for Colonic Drug Delivery. *Int. J. Pharm.* **2000**, *197* (1−2), 181−192.

(3) Goole, J.; Deleuze, Ph.; Vanderbist, F.; Amighi, K. New Levodopa Sustained-Release Floating Minitablets Coated with Insoluble Acrylic Polymer. *Eur. J. Pharm. Biopharm.* **2008**, *68* (2), 310−318.

(4) Nilkumhang, S.; Alhnan, M. A.; McConnell, E. L.; Basit, A. W. Drug Distribution in Enteric Microparticles. *Int. J. Pharm.* **2009**, *379* (1), 1−8.

(5) Park, H.; Otte, A.; Park, K. Evolution of Drug Delivery Systems: From 1950 to 2020 and Beyond. *J. Controlled Release* **2022**, *342*, 53−65.

(6) Lecomte, F.; Siepmann, J.; Walther, M.; MacRae, R. J.; Bodmeier, R. Blends of Enteric and GIT-Insoluble Polymers Used for Film Coating: Physicochemical Characterization and Drug Release Patterns. *J. Controlled Release* **2003**, *89* (3), 457−471.

(7) Glaessl, B.; Siepmann, F.; Tucker, I.; Rades, T.; Siepmann, J. Deeper Insight into the Drug Release Mechanisms in Eudragit RL-Based Delivery Systems. *Int. J. Pharm.* **2010**, *389* (1−2), 139−146.

(8) Goto, S.; Kawata, M.; Nakamura, M.; Maekawa, K.; Aoyama, T. Eudragit RS and RL (Acrylic Resins) Microcapsules as PH Insensitive and Sustained Release Preparations of Ketoprofen. *J. Microencapsulation* **1986**, *3* (4), 293−304.

(9) Cortesi, R.; Ravani, L.; Menegatti, E.; Esposito, E.; Ronconi, F. Eudragit Microparticles for the Release of Budesonide: A Comparative Study. *Indian J. Pharm. Sci.* **2012**, *74* (5), No. 403.

(10) Glaessl, B.; Siepmann, F.; Tucker, I.; Rades, T.; Siepmann, J. Mathematical Modeling of Drug Release from Eudragit RS-Based Delivery Systems. *J. Drug Delivery Sci. Technol.* **2010**, *20* (2), 127−133.

(11) Gendrin, C.; Roggo, Y.; Collet, C. Pharmaceutical Applications of Vibrational Chemical Imaging and Chemometrics: A Review. *J. Pharm. Biomed. Anal.* **2008**, *48* (3), 533−553.

(12) Bonferoni, M. C.; Sandri, G.; Gavini, E.; Rossi, S.; Ferrari, F.; Caramella, C. Microparticle Systems Based on Polymer-Drug Interaction for Ocular Delivery of Ciprofloxacin I. In Vitro Characterization. *J. Drug Delivery Sci. Technol.* **2007**, *17* (1), 57−62.

(13) Doan-Nguyen, V.; Loria, J. P. The Effects of Cosolutes on Protein Dynamics: The Reversal of Denaturant-induced Protein Fluctuations by Trimethylamine N -oxide. *Protein Sci.* **2007**, *16* (1), 20−29.

(14) Velazquez-Campoy, A.; Freire, E. Isothermal Titration Calorimetry to Determine Association Constants for High-Affinity Ligands. *Nat. Protoc.* **2006**, *1* (1), 186−191.

(15) Amponsah-Efah, K. K.; Demeler, B.; Suryanarayanan, R. Characterizing Drug−Polymer Interactions in Aqueous Solution with Analytical Ultracentrifugation. *Mol. Pharmaceutics* **2021**, *18* (1), 246−256.

(16) Lee, J. H.; Okuno, Y.; Cavagnero, S. Sensitivity Enhancement in Solution NMR: Emerging Ideas and New Frontiers. *J. Magn. Reson.* **2014**, *241*, 18−31.

(17) Geppi, M.; Guccione, S.; Mollica, G.; Pignatello, R.; Veracini, C. A. Molecular Properties of Ibuprofen and Its Solid Dispersions with Eudragit RL100 Studied by Solid-State Nuclear Magnetic Resonance. *Pharm. Res.* **2005**, *22* (9), 1544−1555.

(18) Meyvis, T. K. L.; De Smedt, S. C.; Van Oostveldt, P.; Demeester, J. Fluorescence Recovery after Photobleaching: A Versatile Tool for Mobility and Interaction Measurements in Pharmaceutical Research. *Pharm. Res.* **1999**, *16* (8), 1153−1162.

(19) Berk, D. A.; Yuan, F.; Leunig, M.; Jain, R. K. Fluorescence Photobleaching with Spatial Fourier Analysis: Measurement of Diffusion in Light-Scattering Media. *Biophys. J.* **1993**, *65* (6), 2428−2436.

(20) Brown, E. B.; Wu, E. S.; Zipfel, W.; Webb, W. W. Measurement of Molecular Diffusion in Solution by Multiphoton Fluorescence Photobleaching Recovery. *Biophys. J.* **1999**, *77* (5), 2837−2849.

(21) Elias, T. M.; Brown, E. B., Jr.; Brown, E. B., III Expanding the Applicability of Multiphoton Fluorescence Recovery after Photobleaching by Incorporating Shear Stress in Laminar Flow. *J. Biomed. Opt.* **2023**, *28* (7), No. 076502.

(22) Sullivan, K. D.; Majewska, A. K.; Brown, E. B. Single- and Two-Photon Fluorescence Recovery after Photobleaching. *Cold Spring Harbor Protocols* **2015**, *2015* (1), No. pdb.top083519.

(23) Heinze, K. G.; Costantino, S.; De Koninck, P.; Wiseman, P. W. Beyond Photobleaching, Laser Illumination Unbinds Fluorescent Proteins. *J. Phys. Chem. B* **2009**, *113* (15), 5225−5233.

(24) Denk, W.; Strickler, J. H.; Webb, W. W. Two-Photon Laser Scanning Fluorescence Microscopy. *Science* **1990**, *248* (4951), 73−76.

(25) Geiger, A. C.; Smith, C. J.; Takanti, N.; Harmon, D. M.; Carlsen, M. S.; Simpson, G. J. Anomalous Diffusion Characterization by Fourier Transform-FRAP with Patterned Illumination. *Biophys. J.* **2020**, *119* (4), 737−748.

(26) Harmon, D. M.; Cao, Z.; Sherman, A. M.; Takanti, N.; Murati, K.; Wimsatt, M. M.; Cousineau, M. L.; Hwang, Y.; Taylor, L. S.; Simpson, G. J. Diffusion Mapping with Diffractive Optical Elements for Periodically Patterned Photobleaching. *Anal. Chem.* **2024**, *96*. DOI: 10.1021/ACS.ANALCHEM.3C05728.

(27) Cao, Z.; Harmon, D. M.; Yang, R.; Razumtcev, A.; Li, M.; Carlsen, M. S.; Geiger, A. C.; Zemlyanov, D.; Sherman, A. M.; Takanti, N.; Rong, J.; Hwang, Y.; Taylor, L. S.; Simpson, G. J. Periodic Photobleaching with Structured Illumination for Diffusion Imaging. *Anal. Chem.* **2023**, *95* (4), 2192−2202.

(28) Zhu, L.; Jona, J.; Nagapudi, K.; Wu, T. Fast Surface Crystallization of Amorphous Griseofulvin Below T g. *Pharm Res* **2010**, *27*, 1558−1567.

(29) Li, M.; Razumtcev, A.; Turner, G. A.; Hwang, Y.; Simpson, G. J. Fast Diffusion Characterization by Multiphoton Excited Fluorescence Recovery While Photobleaching. *Anal. Chem.* **2023**, *95* (38), 14331−14340.

(30) Sarkar, S.; Song, Z.; Griffin, S. R.; Takanti, N.; Vogt, A. D.; Ruggles, A.; Danzer, G. D.; Simpson, G. J. In Situ Crystal Growth Rate Distributions of Active Pharmaceutical Ingredients. *Mol. Pharmaceutics* **2020**, *17* (3), 769−776.

(31) Arnold, M. M.; Gorman, E. M.; Schieber, L. J.; Munson, E. J.; Berkland, C. NanoCipro Encapsulation in Monodisperse Large Porous PLGA Microparticles. *J. Controlled Release* **2007**, *121* (1−2), 100−109.

(32) Lecomte, F.; Siepmann, J.; Walther, M.; MacRae, R. J.; Bodmeier, R. Polymer Blends Used for the Coating of Multiparticulates: Comparison of Aqueous and Organic Coating Techniques. *Pharm. Res.* **2004**, *21* (5), 882−890.

(33) Rongthong, T.; Sungthongjeen, S.; Siepmann, F.; Siepmann, J.; Pongjanyakul, T. Eudragit RL-Based Film Coatings: How to Minimize Sticking and Adjust Drug Release Using MAS. *Eur. J. Pharm. Biopharm.* **2020**, *148*, 126−133.

(34) Yassin, S.; Su, K.; Lin, H.; Gladden, L. F.; Zeitler, J. A. Diffusion and Swelling Measurements in Pharmaceutical Powder Compacts Using Terahertz Pulsed Imaging. *J. Pharm. Sci.* **2015**, *104* (5), 1658−1667.

(35) Akhgari, A.; Farahmand, F.; Garekani, H. A.; Sadeghi, F.; Vandamme, T. F. Permeability and Swelling Studies on Free Films Containing Inulin in Combination with Different Polymethacrylates

Aimed for Colonic Drug Delivery. *Eur. J. Pharm. Sci.* **2006**, *28* (4), 307–314.

(36) Sun, Y. M.; Hsu, S. C.; Lai, J. Y. Transport Properties of Ionic Drugs in the Ammonio Methacrylate Copolymer Membranes. *Pharm. Res.* **2001**, *18* (3), 304–310.

(37) Bodmeier, R.; Paeratakul, O. Mechanical Properties of Dry and Wet Cellulosic and Acrylic Films Prepared from Aqueous Colloidal Polymer Dispersions Used in the Coating of Solid Dosage Forms. *Pharm. Res.* **1994**, *11* (6), 882–888.

(38) *Aqueous Polymeric Coatings for Pharmaceutical Dosage Forms*; Felton, L. A.; McGinity, J. W.; Felton, L. A., Eds.; CRC Press, 2008.